


Establishment of an empirical force-field for crystalline and amorphous $\text{Li}_2\text{S-SiS}_2$ electrolytesL.-M. Poitras  and M. Micoulaut*Sorbonne Université, Laboratoire de Physique Théorique de la Matière Condensée, CNRS UMR 7600,
4 Place Jussieu, 75252 Paris Cedex 05, France* (Received 3 May 2023; accepted 16 June 2023; published 26 June 2023)

An empirical force-field of Buckingham type is derived for crystalline and glassy $\text{Li}_2\text{S-SiS}_2$ binary alloys using fractional charges, short-range repulsion, and long-range attractive dispersion interactions. Parameters are fitted on low-temperature equilibrium polymorphs Li_2SiS_3 , and permit to recover typical bond distances, cell lengths, and to predict elastic properties. We then use classical molecular dynamics to study the structural properties of corresponding glasses and a very good agreement is found with corresponding data obtained from neutron and x-ray scattering. The resulting glasses are composed of fourfold tetrahedral Si and twofold sulfur, whereas Li atoms experience a more complex environment, partially in defective octahedral or tetrahedral geometry with a coordination number close to three. Unlike the base SiS_2 , the resulting glass network does not contain edge-sharing tetrahedra and displays a rather broad distribution of tetrahedral species that are quantified using the usual Q^n formalism.

DOI: [10.1103/PhysRevB.107.214205](https://doi.org/10.1103/PhysRevB.107.214205)**I. INTRODUCTION**

Fast ion batteries have attracted a broad attention because of their intensive use in mobile phones, electric bikes, scooters, and larger vehicles [1,2]. These setups consist of a Li-based oxide cathode together with an electrolyte that ensures conduction during charge and discharge cycling. As they represent a safety hazard because of the presence of flammable polymeric liquid electrolytes, there have been successful attempts to introduce solid electrolytes instead [3]. Among such solid materials, amorphous or glassy electrolytes [4] are considered as promising candidates because of the possibility to alloy a number of components into base materials, which permits to continuously improve crucial properties such as ionic conduction. While, e.g., binary $\text{Li}_2\text{S-P}_2\text{S}_5$ glasses have now inspired numerous studies because of a high level of conductivity [5–8], silicon based sulfides have received a renewed attention only recently [9,10], largely motivated by their high ionic conduction ($10^{-3} \Omega^{-1} \text{cm}^{-1}$) at ambient conditions (for a review, see Ref. [11]).

Among lithium amorphous chalcogenides, binary $\text{Li}_2\text{S-SiS}_2$ glasses with varying Li content have been characterized by a variety of techniques [12–19].

In the goal of designing new glassy electrolytes for battery applications, computational techniques such as *ab initio* or classical molecular dynamics (MD) simulations are useful tools for calculating physicochemical properties since they allow for a comprehensive link between the atomic scale description, that is, structure, and calculated ensemble averaged quantities. A certain number of efforts have been performed in this direction from classical modeling [20–22] or reverse Monte Carlo simulations [7]. The most “recent” effort [22] is now quite old (1996) and led unfortunately to some spurious results such as fivefold Si atoms in the glassy state, the experimental data for the validation of the force-field being rather sparse at that time [23] or maybe overlooked [24]. Since then, there have been different scattering experiments (x-ray [10]

or neutron [25,26]) on various compositions in the $\text{Li}_2\text{S-SiS}_2$ system, and these experiments actually completely rule out the force-field established previously. There is, therefore, an opportunity for considering a new effort in this direction.

Here, we provide a generalized self-consistent pairwise force-field able to model the structural properties of $\text{SiS}_2\text{-Li}_2\text{S}$ glasses and crystals. While such force-fields are very common in oxides, we have stated previously that investigations concerning thiosilicates are rather limited (see, however, Ref. [27]), albeit some simple phenomenological models have been proposed but with a limited output [28,29]. Numerical approaches usually assume that atomic forces in crystals and corresponding glasses must be of the same order of magnitude so that a force-field able to capture the salient atomic interactions in the crystalline structure should be able to describe the liquid and the glassy phase as well. Such investigations have been performed for certain isochemical compounds [30–32] such as α quartz and silica and subsequent modified silicates. This permits to fit interatomic potentials from a series of crystals and from mechanical observables (e.g., bulk and shear modulus), the latter providing some information on the potential energy curvature.

In this contribution, we build on the method used by Pedone and coworkers [30] to generate the potential functions for $\text{SiS}_2\text{-Li}_2\text{S}$. We fit empirically the crystal structure data of Li_2SiS_3 within the general utility lattice program (GULP) and zero forces [33–35], in conjunction with a relaxation technique and a vibrational eigenmode calculation that permits to select among fitted parameters those which lead to stable crystalline structures at ambient temperature. The obtained structures are discussed and compared with experimental measurements, prior to an investigation of the glassy state. This permits to validate the parameters as both structure factor $S(k)$ and pair correlation function $g(r)$ are now reproduced with a rather satisfying accuracy. The detail of the atomic scale trajectories then reveals the short- and intermediate-range order of such important glasses for energy applications.

II. METHODOLOGY

A. General framework

In the GULP approach [35], the interaction potential parameters are obtained from experimental reported crystal structures that lead to the reproduction of atomic positions, density or lattice parameters. Here, we use the Buckingham potential that contains a strong repulsive interaction arising from the electrostatic repulsion at short distances, a Coulomb interaction, and a long-range attractive dispersive interaction,

$$V_{ij}(r) = A_{ij}e^{-r/\rho_{ij}} + \frac{q_i q_j}{r} - \frac{C_{ij}}{r^6}. \quad (1)$$

In the binary lithium thiosilicate alloy, three crystalline polymorphs have been identified. In the lithium-rich region a Li_4Si_4 phase forms from a direct comelting of Li_2S and SiS_2 in 2:1 ratio, and melts congruently at $T_m = 983 \pm 20$ K [36–38]. At reduced Li content (50:50), at least two orthorhombic Li_2SiS_3 phases occur: A first one, which is metastable (m- Li_2SiS_3) with a melting temperature of $T_m = 1018 \pm 10$ K [37] and an equilibrium phase (e- Li_2SiS_3), which is obtained upon rapid cooling to 993 K with subsequent annealing at the same temperature [38,39]. As in the corresponding silicate, the resulting network of both phases is thought to be made of corner-sharing tetrahedra using so-called Q^2 units, i.e., tetrahedra having two bridging and two nonbridging (NBS) sulfur, the latter being in the vicinity of Li ions whereas the former is responsible for the one-dimensional chain structure of Li_2SiS_3 via bridging sulfur (BS) atoms that connect to two adjacent Si atoms. For completeness, we should also mention a more recent structure (n- Li_2SiS_3), which is tetragonal and contains phosphorus impurities [40]. It should also be noted that the e- Li_2SiS_3 is only conjectured as it results from a simulated x-ray powder measurement using the appropriately rescaled atomic coordinates of Li_2SiO_3 as input parameters [37]. As a matter of fact, the structure of e- Li_2SiS_3 might differ from m- Li_2SiS_3 as ^{29}Si magic angle spinning nuclear magnetic resonance experiments have suggested the presence of edge-sharing $\text{SiS}_{4/2}$ tetrahedra [41]. However, the exact atomic coordinates of this “true” phase being unknown, we will work with the one proposed from Li_2SiO_3 .

As an initial guess for crystalline e- Li_2SiS_3 , we have used the potential parameter proposed by Seshayasee and Muruganandam [22] for the description of the 50 SiS_2 -50 Li_2S glass (g- Li_2SiS_3). Note that the other crystal structure of the binary Li_2S - SiS_2 alloy has not been considered (Li_4SiS_4) as the atomic positions in the unit cell continue to be speculative [37]. Then, we have followed a fitting procedure [35], which minimizes a weight function,

$$F = \sum_{i=k}^M (C_{\text{calc}}(k) - C_{\text{obs}}(k))^2 \quad (2)$$

with M observables $C_{\text{obs}}(k)$ being the atomic coordinates of the crystalline elementary cells [37–39] and the forces set to zero. The fitting procedure, i.e., the variation of the potential parameters so as to get the positions with zero forces, stops when the energy gradient becomes lower than a certain value (typically 0.01 a.u.). In the GULP procedure, this default strategy can be improved by adding observables such

TABLE I. Buckingham parameters of Eq. (1) that describe crystalline e- and m- Li_2SiS_3 . Charges have been taken as $q_{\text{Si}} = 2.4e$, $q_{\text{S}} = -1.2e$, and $q_{\text{Li}} = 0.6e$.

Atom i	Atom j	A_{ij} (kJ mol $^{-1}$)	ρ_{ij} (Å)	C_{ij} (kJ mol $^{-1}$ Å $^{-6}$)
Si	Si	200678290.92765	0.072	
Si	S	7718820.0	0.178	
Si	Li	528220069.276	0.076	
S	S	10613383.8	0.284	96485.0
S	Li	9648530.75	0.182	
Li	Li	677340912.466	0.080	

as, e.g., elastic constants or bulk moduli, which represent second derivatives of the energy. However, since mechanical or optical observables (high-frequency and static dielectric constants) have never been reported for such crystalline thiosilicates, one cannot rely on such additional observables to constrain the curvature of the energy surface as, e.g., performed in alkali silicates [30]. In order to take into account the fact that the fitting is performed at 300 K, thermal forces are explicitly included in the GULP code by means of a Gibbs free energy minimization [33], rather than an energy minimization. This technique termed as *relaxed fitting* leads to a slight change in atomic positions.

An additional way to constrain the minimization process is to run simultaneously to the Gibbs free energy minimization a calculation of the $3N$ vibrational eigenmodes ω_i of the structure that are determined [42] from the eigenvalues of the dynamical matrix where the sum runs over the relative position change R of distance r_{ij} under the influence of a vibration,

$$D_{i\alpha j\beta} = \frac{1}{\sqrt{m_i m_j}} \sum_R \frac{\partial^2 V}{\partial \alpha \partial \beta} e^{ik(r_{ij}+R)} \quad (3)$$

with the requirement that most (if not all) all vibrational modes (phonons) satisfy $\omega_i > 0$. This ensures that second derivatives with respect to the atoms in Cartesian space (i.e., the force constant matrix) are positive and lead to stable vibrations. The lowest three modes are zero at the center of the Brillouin zone (Γ point), and these correspond to the pure translation of the crystal lattice, identified with the acoustic branch.

These requirements and constraints led to a satisfying convergence of the parameters of Eq. (1), that were constrained in addition to obtain a correct structure for the corresponding glassy state and satisfying zero pressure at the glass density (Table I). These involve essentially a Coulomb and a repulsive part, the only dispersion potential being present for the S-S interaction, which is compatible with the presence of van der Waals forces maintaining chains of edge-sharing tetrahedra in the base glass [43] or in the metathiosilicate polymorph [37].

B. Molecular dynamics

Once the parameters are fixed, classical molecular dynamics (MD) simulations in NVT and NPT ensemble have been performed on a crystalline e- and m- Li_2S - SiS_2 and a glassy system containing $N = 3000$ atoms (i.e., $N_{\text{Li}} = 1000$, $N_{\text{Si}} = 500$, and $N_{\text{S}} = 1500$, Fig. 1). The initial crystalline structure

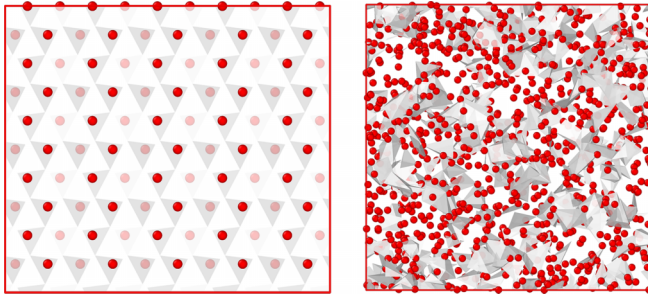


FIG. 1. Atomic snapshot of crystalline (left) $e\text{-Li}_2\text{SiS}_3$ and glassy Li_2SiS_3 (right). Si tetrahedra are marked in gray, Li atoms are red.

has been obtained by replicating five times the elementary cell in each direction, whereas the liquid-glass configuration has been generated by adding atoms randomly to a cubic simulation box of side length 39.26 \AA matching the experimental density of the glass [10] (0.0494 \AA^{-3}). These initial configurations have served to either melt the crystalline structure to verify the melting process of $e\text{-Li}_2\text{S-SiS}_2$ or to quench a glass from a high temperature liquid at different cooling rates. To integrate the equations of motion, we have used a Verlet algorithm with time step $\Delta t = 1 \text{ fs}$. The cubic box has been maintained at 2000 K during 100 ps , prior to a quench at a cooling rate of 1 K/ps to 300 K in NPT and NVT ensemble. Statistical analysis of the glass has been performed in NVT over 100 ps , the differences in structures between both ensembles being small given the small residual pressure obtained (-0.10 GPa , see Table II). At a local level, there is no difference in composition with respect to the nominal one (Li_2SiS_3) that might result from the force-field since we have performed a high-temperature homogenization of the system, and the resulting local structure is indeed tetrahedral with four sulfur atoms around a Si atom (see below). Rather than coupled force-field/system size effects, certain resulting glasses with coordination changes induced by charge compensation can display small variations due to thermal history effects (see e.g., Ref. [44]), but these effects are absent in the present thiosilicate system.

III. RESULTS AND DISCUSSION

A. Crystalline Li_2SiS_3

We first focus on the two phases of Li_2SiS_3 whose structural parameters are given in Table II. In NPT with fixed zero pressure, a slight increase of all cell lengths (a , b , and c) is acknowledged, and this results from a residual pressure that is detected at fixed simulation box conditions (NVT). The residual pressure is reduced in $m\text{-Li}_2\text{SiS}_3$ given the increased cell lengths [39] with respect to the equilibrium phase [37]. The existence of a rather important residual pressure in NVT for $e\text{-Li}_2\text{SiS}_3$ might have at least two possible origins. First, we remind that the proposed coordinates of this polymorph are only conjectured as they are only based on an analogy of the well-documented Li_2SiO_3 phase [45]. A possible incorrect structure for the sulfur compound could lead to nonzero residual pressure. Secondly, the GULP procedure has been performed on a structure with zero forces, which can also

TABLE II. Experimental cell parameters [37–39] (in \AA), residual pressure, system density n_0 , and main distances of $m\text{-Li}_2\text{SiS}_3$ and $e\text{-Li}_2\text{SiS}_3$ at 300 K , together with data from the glassy state ($g\text{-Li}_2\text{SiS}_3$), compared to calculated values from Eq. (1) in NPT and NVT ensemble at the same temperature. Bond distances of $m\text{-Li}_2\text{SiS}_3$ are not given as they are very close to those of $e\text{-Li}_2\text{SiS}_3$ (see Fig. 2).

	Expt.	NVT	NPT
$e\text{-Li}_2\text{SiS}_3$			
a (\AA)	11.664 [37]		11.754
b (\AA)	6.735 [37]		6.787
c (\AA)	5.926 [37]		5.971
n_0 (\AA^{-3})	0.0515 [37]	0.0515	0.0579
P (GPa)		-7.00	0
$d_{\text{Si-S}}$ (\AA)	2.09	1.94	2.08
$d_{\text{S-S}}$ (\AA)	3.36	3.26	3.48
$d_{\text{Li-S}}$ (\AA)	2.46	2.42	2.45
$m\text{-Li}_2\text{SiS}_3$			
a (\AA)	11.436 [39]		11.318
b (\AA)	6.605 [39]		6.420
c (\AA)	6.487 [39]		6.537
n_0 (\AA^{-3})	0.0489 [39]	0.0489	0.0505
P (GPa)		-1.80	0
$g\text{-Li}_2\text{SiS}_3$			
n_0 (\AA^{-3})	0.0494 [7]	0.0494	0.0496
P (GPa)		-0.10	0
$d_{\text{Si-S}}$ (\AA)	2.20 [25]	2.11	2.11
	2.16 [23]		
$d_{\text{S-S}}$ (\AA)		3.46	3.46
$d_{\text{Li-S}}$ (\AA)	2.49 [25]	2.47	2.47
$d_{\text{Si-Si}}$ (\AA)		4.05	4.05
$d_{\text{Li-Li}}$ (\AA)		3.05	3.06
$d_{\text{Si-Li}}$ (\AA)		3.87	3.87

lead, once the parameters being fixed, to a residual pressure at the experimental density. We note, however, that once the parameters are fixed, $m\text{-Li}_2\text{SiS}_3$ involve a pressure P that is much smaller (-1.80 GPa), and for glassy Li_2SiS_3 the pressure is nearly zero.

The main bond distances are now reproduced with a pair correlation profile (Fig. 2) that mimics the one of the initial crystalline cell. The principal peaks are, indeed, reproduced among which the Si-S bond distance [37] (2.09 \AA versus 2.08 \AA in NPT) and the Li-S, which corresponds to the bond length between a lithium ion and a nonbridging sulfur (2.45 \AA versus 2.46 \AA). The Si-Si distance arises from the correlation between two atoms belonging to the corner-sharing chain of Q^2 units, the chain character being revealed by a periodic distance found at 6.7 \AA and 9.0 \AA . The sulfur-sulfur distance arises from the $\text{SiS}_{4/2}$ tetrahedral edges ($3.26\text{--}3.48 \text{ \AA}$, consistently with the distance found in the base SiS_2 crystal [43] $\{3.27 \text{ \AA}\}$). The usual tetrahedral characteristic parameter, i.e., $\delta = d_{\text{Si-S}}/d_{\text{S-S}}$ is found to be very close to the expected value $\sqrt{3/8} = 0.612$ for a perfect tetrahedron, and this is the case for both experimental data ($\delta = 0.622$) and simulation ($\delta = 0.598$ in NPT, 0.595 in NVT). These results indicate that the potential Eq. (1) takes into account the tetrahedral character of the Si atoms, in contrast with the initial set of parameters [22].

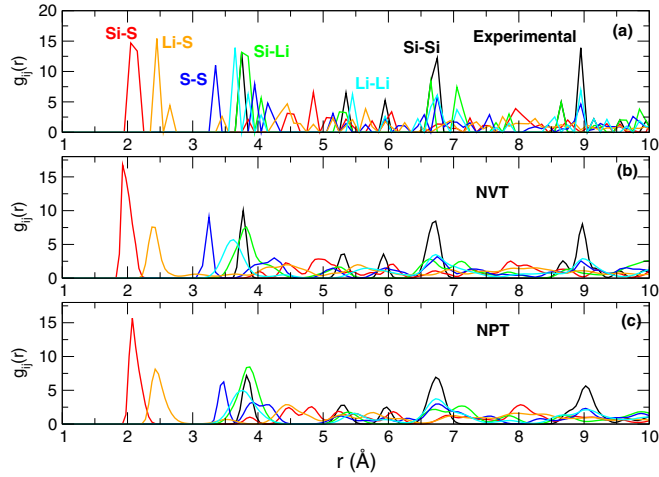


FIG. 2. Calculated partial pair correlation functions $g_{ij}(r)$ of e- Li_2SiS_3 from the elementary cell determined by Ahn and Huggins [37] (a), from the NVT (b), and NPT (c) $N = 3000$ simulation box.

An inspection of the bond angle distributions (BAD) also indicates the dominant tetrahedral character of Si in the different phases [Fig. 3(a)] with a S-Si-S distribution that peaks at $\arccos(-\frac{1}{3}) \simeq 109^\circ$. The intertetrahedral connection (Si-S-Si) is sensitive to the structure with a progressive shift from 120° in e- Li_2SiS_3 to 131° in m- Li_2SiS_3 , which is compatible with the angle of 138° proposed by Ahn and Huggins [39]. The local Li environment appears to be nearly tetrahedral as well with a S-Li-S BAD centered at 109° as well, albeit in defective geometry given the calculated coordination number (see below) and $d_{\text{Li-S}}/d_{\text{S-S}} = 0.71$, which suggests [46] a slightly distorted tetrahedra ($d_{\text{Li-S}}/d_{\text{S-S}} \neq \sqrt{8/3}$).

1. Elastic properties

From the potential [Eq. (1)] and the different atomic configuration, the elastic tensor \mathbf{C} can be evaluated from the second derivative of the energy with respect to infinitesimal strain components established along the three Cartesian coor-

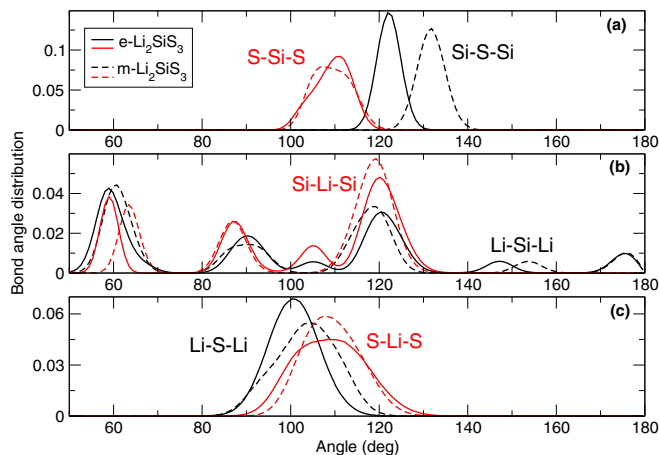


FIG. 3. Calculated bond angle distribution in e- Li_2SiS_3 (solid lines) and m- Li_2SiS_3 (broken lines).

TABLE III. Calculated Voigt elastic properties for the two crystalline phases and for the glass: Longitudinal C_{11} and transverse elastic constants C_{44} , elastic constant C_{12} , bulk modulus B , shear modulus G , and compressibility χ_T .

	e- Li_2SiS_3	m- Li_2SiS_3	g- Li_2SiS_3
C_{11} (GPa)	86.8	43.6	80.3
C_{12} (GPa)	50.3	10.7	36.1
C_{44} (GPa)	26.3	2.03	22.7
B (GPa)	58.8	18.5	50.33
G (GPa)	23.9	12.2	22.4
χ_T (GPa^{-1})	0.017	0.057	0.020

dinates on the atomic configuration [33,47],

$$C_{ij} = \frac{1}{V} \left(\frac{\partial^2 E}{\partial \epsilon_i \partial \epsilon_j} \right), \quad (4)$$

out of which the compliance matrix \mathbf{S} can be calculated from $\mathbf{S} = \mathbf{C}^{-1}$, which permits to estimate the bulk modulus in Reuss notation via

$$B^{-1} = S(1, 1) + S(2, 2) + S(3, 3) + 2[S(3, 1) + S(2, 1) + S(3, 2)] \quad (5)$$

and the shear modulus

$$G = \frac{15}{Z} \quad (6)$$

with

$$Z = 4(S_{11} + S_{22} + S_{33} - S_{12} - S_{13} - S_{23}) + 3(S_{44} + S_{55} + S_{66}). \quad (7)$$

For the present systems, the different relevant elastic constants have been computed from different configurations (crystal or glassy) by means of the GULP code [35] after a Newton-Raphson energy minimization at fixed volume. For g- Li_2SiS_3 , given its amorphous character, the calculation has been performed without any symmetry (space group P_1). Results are given in Table III. We are not aware of any elastic measurement of Li_2SiS_3 but like to mention that these are important for the understanding of ion transport since the mobility of the charge carriers is linked with the elastic deformation of the network.

An inspection of the obtained values suggests a possible overestimation of the elastic constants as, e.g., bulk modulus such as Ge-Se glasses is usually of the order of $B \simeq 20$ GPa [48], albeit certain recent *ab initio* simulations of crystalline chalcogenides found B to be of about 70–90 GPa [49]. The interest of Table III is more likely to provide, for the model potential [Eq. (1)], a relative comparison between the crystal and the glass of same composition, which suggests here a similar mechanical behavior between e- and g- Li_2SiS_3 . The ratio G/B between shear and bulk modulus is found to be of the order of 0.40–0.65 for the three considered structures, which is the range of ratios observed in a series of chalcogenide alloys (0.57 [49]), which also depend substantially on the nature of the chemical bonding.

For a similar electrolyte ($\text{Li}_2\text{S-P}_2\text{S}_5$), the shear modulus is of about 7–8 GPa in the crystalline state [50], i.e., slightly

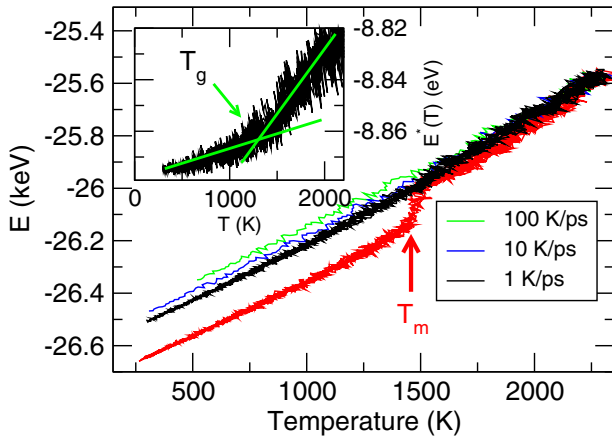


FIG. 4. Potential energy $E(T)$ of e- Li_2SiS_3 (red) as a function of temperature T , together with quenched liquids at different cooling rates (1–100 K/ps). The change in slope (inset, 1K/ps) in the reduced energy $E^*(T)$ locates the glass transition.

higher than the one measured for corresponding glasses. These values are still much smaller than those determined (Table III) although it has been reported that Si-substituted thiophosphates have slightly larger moduli due to a greater ionic character of bonding [51].

The comparison with corresponding alkali silicates indicates that C_{11} and C_{44} are of the same order of magnitude as values of about 70–80 GPa and 20–30 GPa have been reported [52] for C_{11} and C_{44} in glassy Li_2SiO_3 , respectively. Simulation results on the lithium silicate compounds using the same methodology [35] from numerical simulations confirm the experimental values of silicates and are in line [53] with those determined for the present thiosilicate, i.e., $B \simeq 55$ GPa, $G \simeq 31$ GPa, and a Young modulus $E \simeq 78$ GPa. We found $E = 58$ GPa for the Li_2SiS_3 glass, a value that is larger than the one found in $\text{Li}_2\text{S-P}_2\text{S}_5$ (18–25 GPa [54]). This still satisfies the overall property that chalcogenide elastic constants are lower than those of corresponding oxide glasses, and can be understood from the simple fact that sulfides have, indeed, a lower bond dissociation energy per unit volume and a lower ion packing density.

2. Melting and quenching

Having set and validated the parameters, the melting of the system can now be considered. Figure 4 represents the isochoric energy $E(T)$ for the system with heating and different cooling rates ($q = 100$ K/ps, 10 K/ps, 1 K/ps), together with the reduced energy $E^*(T) = E(T) - \frac{3}{2}k_B T$ (inset) for $q = 1$ K/ps. Note that the factor $\frac{3}{2}k_B T$ is subtracted from the energy, which accounts for base phonon (harmonic motions) at low temperature. One identifies clearly from the heating curve the melting point, at $T_m = 1490$ K (1018 K experimentally [37]). The detail of the energetic contributions (not shown) permits to detect that the Li subnetwork drives the melting with a marked change of $E(T)$ at T_m that contrasts with the energy evolution of the (Si,S). This situation appears to be different with the one observed in, e.g., sodium silicates for which the alkali subnetwork is melting before the silica one [55]. We assign the difference to the rather important melting temperature

difference between silica and corresponding alkali oxides, which corresponds to a situation not met in thiosilicates.

A subsequent quenching of the liquid leads to the usual phenomenology of the glass transition from numerical simulations [56,57], i.e., a decrease of the energy with temperature, and a system falling out of equilibrium at lower energy (and lower T) when the liquid is cooled at a more reduced cooling rate (Fig. 4). While the glass transition is barely detected because of the dominant harmonic motions, which lead to the near linear behavior of $E(T)$, the reduced $E^*(T)$ permits to blow up an obvious change in slope at the glass transition [56], which depends on the applied cooling rate. Here, we find from the intercept of the low- and high-temperature behavior of $E^*(T)$ at 1 K/ps a glass transition temperature of $T_g \simeq 1300$ K (experimentally $T_g = 593$ K [39]). We recover here the usual discrepancies between simulated and experimental glass transition temperatures that can be explained by the ultrafast numerical quenching rates (10^{12} K/s) compared to those applied [11] in thiosilicates (10^6 K/s). The apparent difference is also linked with size effects, and these can be quantified from a model of heat transfer, which predicts that typical cooling rates are linked to the volume V over area A ratio via a log-log relation [58] $\ln q \propto V/A \propto L$. The main qualitative outcome is that for micrometric systems (e.g., water [59]) cooling rates of about 10^6 K/s are required, and for nanometric (MD) ones, 10^9 K/s.

B. Glass structure

The obtained structure using the potential and parameters of Table I can now be compared to experimental data in the glassy state. We first calculate the total weighted structure factor $S(k)$, which is derived using the partial correlations $S_{nm}(k)$,

$$S(k) = \langle f \rangle^{-2} \sum_{n,m} c_n c_m f_n f_m S_{nm}(k) \quad (8)$$

with

$$\langle f \rangle = \sum_n c_n f_n = x_{\text{Si}} f_{\text{Si}} + x_{\text{S}} f_{\text{S}} + (1 - x_{\text{Si}} - x_{\text{S}}) f_{\text{Li}} \quad (9)$$

where the f_n represent either the atomic form factors ($f_{\text{Si}} = 14$, $f_{\text{S}} = 16$, $f_{\text{Li}} = 3$) in x-ray scattering, or the neutron scattering lengths ($f_{\text{Si}} = 4.149$ fm, $f_{\text{S}} = 2.847$ fm, $f_{\text{Li}} = -1.900$ fm) in neutron scattering. Here c_n represent the species concentration, respectively, i.e., $c_{\text{Si}} = 0.167$, $c_{\text{S}} = 0.500$ and $c_{\text{Li}} = 0.333$. The partial and total correlations in Fourier space have been evaluated from a Fourier transform of the partial pair correlation functions,

$$S_{nm}(k) = 1 + n_0 \int_0^\infty 4\pi r^2 [g_{nm}(r) - 1] \frac{\sin(kr)}{kr} dr \quad (10)$$

where n_0 is the system density [10]. Using the numbers provided, we can calculate a XRD weighted function,

$$S_X(k) = 0.498S_{\text{SS}} + 0.291S_{\text{SiS}} + 0.124S_{\text{LiS}} \\ + 0.042S_{\text{SiSi}} + 0.036S_{\text{SiLi}} + 0.008S_{\text{LiLi}} \quad (11)$$

and a ND weighted function

$$S_{\text{ND}}(k) = 0.920S_{\text{SS}} + 0.896S_{\text{SiS}} - 0.818S_{\text{LiS}} \\ + 0.218S_{\text{SiSi}} - 0.398S_{\text{SiLi}} + 0.182S_{\text{LiLi}}. \quad (12)$$

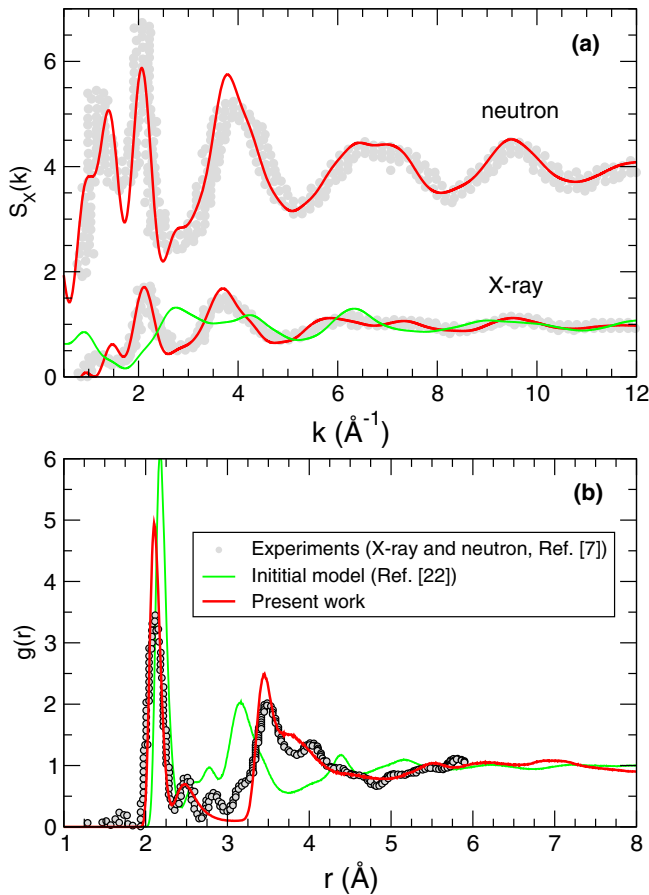


FIG. 5. (a) Calculated neutron and x-ray structure factor $S(k)$ of amorphous Li_2SiS_3 (red curves), compared to experiments [7] (gray circles) from neutron and x-ray scattering, and to the initial potential [22] (green curves). (b) Calculated pair correlation function $g(r)$ (red curves), compared to experiments from x-ray scattering [7] (circles) and to the results from the initial potential [22] (green).

The calculated $S(k)$ from the potential permits to recover peak positions and appear to be in very good agreement with the measured total structure factor [Fig. 5(a)] for both x-ray and neutron scattering [7,25], albeit the intensity of the first principal peak at $k_1 = 1.25 \text{ \AA}^{-1}$ in the neutron $S_N(k)$ is slightly underestimated. The other principal peaks at $k_2 \simeq 2.1 \text{ \AA}^{-1}$ and $k_3 = 4.0 \text{ \AA}^{-1}$ are also reproduced with an excellent accuracy, as are the oscillations at larger momentum transfer k , in obvious contrast with the potential parameters proposed by Seshayasee and Muruganandam (green curve [22]). The same level of agreement is achieved for the x-ray structure factor $S_X(k)$ and it has to be noted that the improvement is substantial when our results using Table I are compared to those obtained from the potential initially parametrized [22], which leads to a rather poor reproduction of the experimental data (green curves, Fig. 5). In real space, the same conclusion can be made and the present potential is able to reproduce the x-ray weighted pair correlation function $g(r)$ over the entire experimental range ($r \leq 6 \text{ \AA}$), in contrast with the previous potential, which overestimates the principal peak position arising from the Si-S correlations, and underestimates the second correlating distance, which is produced by S-S bonds.

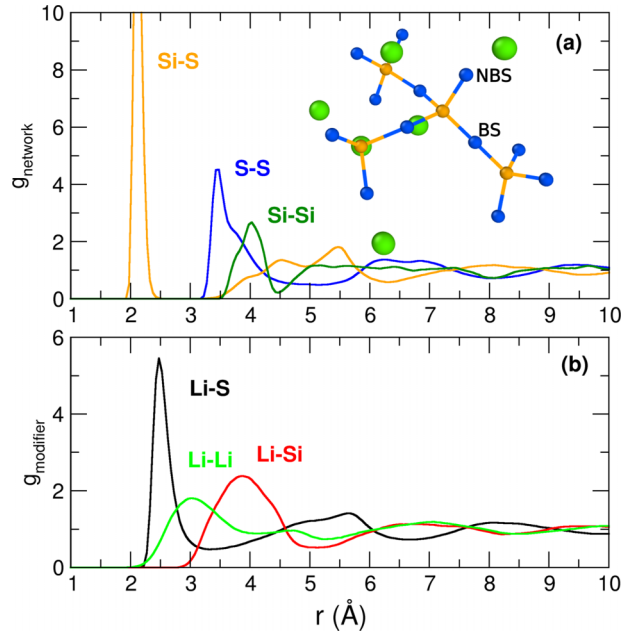


FIG. 6. Calculated partial correlation functions $g_{ij}(r)$ of glassy Li_2SiS_3 , decomposed into network contributions (a) and Li-related ones (b). In (a), a typical molecular fragment of $g\text{-Li}_2\text{SiS}_3$ is represented with BS and NBS atoms present in a series of connected Q^4 , Q^3 , and Q^2 tetrahedra.

Our numerical data reproduces the position and amplitude of both main peaks with a satisfying accuracy (2.11 \AA vs 2.13 \AA [7,25,26] and 3.46 \AA vs 3.49 \AA), but apparently reduces a ternary peak observed at $\simeq 4.0 \text{ \AA}$ to a shoulder peak at a distance somewhat smaller than 4.0 \AA . We, furthermore, note that the experimental data contains two small peaks (between 2.5 \AA and 3.0 \AA) that are only partially reproduced. While this might be a limitation of the potential, we note that the experimental data [7] contains large ripples arising from the Fourier transform at finite k , and which might extend up to these distances.

1. Partial correlations

The partial correlations can now be established and these provide additional information into the structure of $g\text{-Li}_2\text{SiS}_3$. Figure 6 represents the pair correlation functions $g_{ij}(r)$ that have been splitted into a network part (a) and the Li-related partials (b). Corresponding bond lengths [maximum of each $g_{ij}(r)$] are given in Table II. While the principal peak corresponds, indeed, to the Si-S distance (2.11 \AA) and leads to the principal peak of the total $g(r)$ function [Fig. 5(b)], it can be noted that secondary correlations arise from different contributions: S-S (3.46 \AA) and Si-Si (4.05 \AA) to a lesser extent, together with Li-Si (3.87 \AA) and Li-Li (3.06 \AA), the latter distance being compatible with the one determined [60] in the corresponding oxide compound ($2.87\text{--}3.26 \text{ \AA}$). The dominant bond length in Li-related partials is clearly the one associated with Li-S correlations that maximize at 2.47 \AA . These agree with measurements from neutron scattering [25] and with the value determined [61] in the Li_2S crystal (2.47 \AA). Our determined Li coordination number is $n_{\text{LiS}} = 2.94(6)$ is consistent with the estimate from neutron scattering [25] ($n_{\text{LiS}} = 3.0$) but

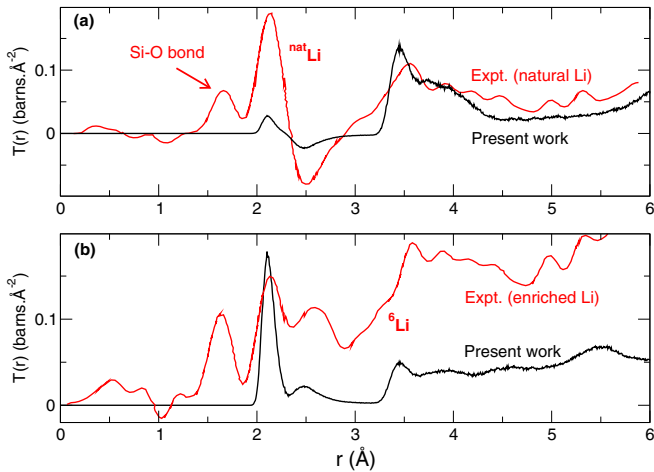


FIG. 7. Calculated neutron pair correlation function $g_N(r)$ (black) of natural Li (a) and isotopically ^6Li enriched (b) glassy Li_2SiS_3 , compared to experimental data [25,26] (red). Note (i) the presence of a Si-O bond at 1.62 Å which indicates important water/air pollution of the system and (ii) absence of full information on experimental setup and differential cross sections so that calculated and experimental functions cannot be directly compared, except for the peak positions.

slightly smaller than the value of 4.1 that has been determined independently from scattering data [24] that involved a rather large Li-S distance (2.7 Å). The potential leads to coordination numbers of Si and S that are equal to 4 and 2, respectively.

As natural Li has a neutron coherence length of $b_{\text{Li}} = -1.9$ fm, it leads to a pronounced effect in pair correlation functions that can be also investigated by from enriched samples using the ^6Li isotope. The corresponding scattering function [Eq. (12)], indeed, modified with $f_{\text{Li}} = b_{\text{Li}} = 1.4$ fm, is equal to

$$S_{ND}^6(k) = 0.304S_{\text{SS}} + 0.0.296S_{\text{SiS}} + 0.199S_{\text{LiS}} + 0.072S_{\text{SiSi}} + 0.097S_{\text{SiLi}} + 0.033S_{\text{LiLi}}. \quad (13)$$

Due to the difference in neutron coherence length, resulting total pair correlation functions of natural and enriched glasses [25,26] reveal the contributions of Li (Fig. 7). It is interesting to note that the potential (1) is able to reproduce qualitatively the main features of the pair correlation function, i.e., for natural Li a dominant peak corresponding to the Si-S distance followed by a negative contribution (panel a) arising from Li crossed correlations (Li-Si and Li-S) at $r \simeq 2.5$ Å, as these have a negative neutron coherence length [Eq. (12)]. We have identified the latter with Li-S correlations [Fig. 6(b)], the typical distances involved in Si-Li being detected at larger distances. This Li-S contribution becomes positive for the enriched system [Fig. 7(b)] and our calculated $g_N(r)$ also qualitatively reproduces all peaks. There is, therefore, a good confidence that the fitted potential is not only able to describe the network character of $g\text{-Li}_2\text{SiS}_3$ but also the Li environment.

2. Angles and base geometries

We have stressed the Si tetrahedral character obtained from the potential (1) in the crystalline phases, and this is also

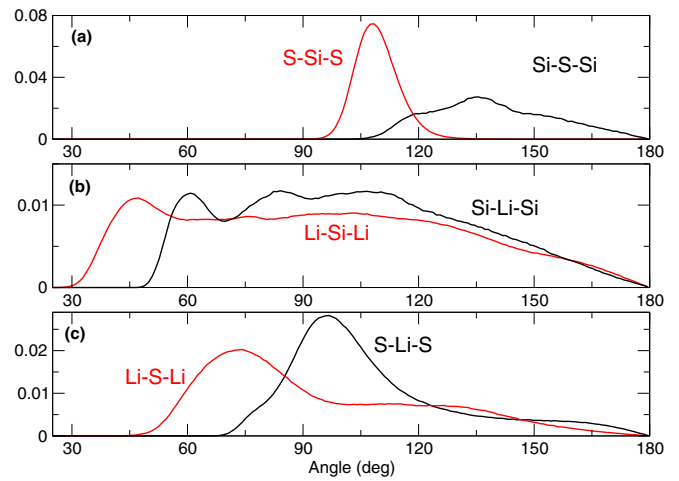


FIG. 8. Calculated bond angle distribution of $g\text{-Li}_2\text{SiS}_3$ at 300 K. Network-related (a), Li-Si related (b), and Li-S related (c).

maintained in the glassy phase (Fig. 8). The S-Si-S bond angle distribution (BAD) is, indeed, found to be centered at 109° as in many other tetrahedral network-forming glasses [62–64]. Conversely, the Si-S-Si bond angle (which involves, by definition the BS atoms) displays a broad BAD centered at $\simeq 130^\circ$ that is similar to the one encountered in, e.g., alkali silicates [65,66]. In the glass, lithium atoms occupy a near tetrahedral site, which manifests in the S-Li-S BAD by an obvious pronounced peak centered at 109° [Fig. 8(c)] as in the corresponding crystal [Fig. 3(c)], although we also note an important contribution close to 180° that is usually the signature of (possibly defective) octahedral environments [67]. Given the determined coordination of Li ($n_{\text{Li}} = 2.94$), however, these sites appear to be defective in character, i.e., the lithium ions are slightly displaced from the center of the tetrahedra and this leads to a [3 + 1] coordination environment with long and short bonds. In character, the Li ions thus have the same environment as those analyzed [60] in the Li_2SiO_3 compound. Finally, we note various bond angle correlations between the network species Si and Li, which leads to a broad BAD for both Li-Si-Li and Si-Li-Si triplets [Fig. 8(b)].

3. Edge-sharing population

As the base glass SiS_2 is believed to be made of chains of edge-sharing $\text{SiS}_{4/2}$ tetrahedra [68,69] (a $n = 4$ ring), one might wonder if such structural fragments are still present once the network has been disrupted by lithium sulfide. Such fragments are thought to have a specific signature in ^{29}Si NMR and results [16,70] for a series of $x\text{Li}_2\text{S}-(1-x)\text{SiS}_2$ glasses have shown that for $0 \leq x \leq 40\%$ Li_2S the fraction of edge-sharing units decreases continuously before reaching a near constant value for larger Li content. The proportion [16] of edge-sharing tetrahedra is about 23% in $g\text{-Li}_2\text{SiS}_3$, and this might indicate that the glass structure maintains a partial chain-like structure with the base tetrahedra $\text{SiS}_{4/2}$ being connected both by edges and corners.

Using a ring statistics algorithm, which builds on a rigorous investigation of networks generated using simulation (RINGS) code [71], we determine from the glass structure

TABLE IV. Calculated fraction of Q^n distribution (in %) in $g\text{-Li}_2\text{SiS}_3$, and compared to various models from the literature. Note that the NMR data on silicates [76] apply on 40% modified silica (no Li_2SiO_3 data available).

	Q^4	Q^3	Q^2	Q^1	Q^0
Present work	5.8	20.7	35.4	30.6	7.5
Topological model [29]	8.6	19.2	35.2	36.8	
^{29}Si NMR [16]	50.0		50.0		
Ideal chemical model			100.0		
Silicate (^{29}Si NMR) [76]	16.0	57.0	25.0		
Silicate (MD) [65]	4.0	24.0	43.4	23.0	4.2

the fraction of such edge-sharing motifs and the concentration of small rings. A cutoff distance of 2.80 Å is been used for all atomic pairs, corresponding to the minimum of the pair correlation function [Fig. 5(b)]. The algorithm is mostly based on the King [72], Franzblau [73] shortest-path search to find rings containing a maximum of 14 atoms. The statistics over the (Si,S) network indicates a near complete depolymerization of the network with a complete absence of small rings, the smallest ring sizes being $n = 8$ (8 ± 1 rings among the 2000 atomic Si-S subnetwork), $n = 10$ (8 ± 2), and $n = 12$ (6 ± 2). One can, thus, conclude that edge-sharing tetrahedra are virtually absent for the Li_2SiS_3 composition, although one should keep in mind that in other glass-forming systems the nucleation of rings in numerical studies is obviously tied to activation barriers [74,75] and to typical times that are beyond the available computer timescale.

4. Q^n speciation

An interesting means for the analysis of modified glasses uses the Q^n terminology, which represents the population of Si tetrahedra having n bridging sulfur (BS) that can be accessed by solid state nuclear magnetic resonance (^{29}Si NMR [11,16,41,70]). As already pointed out in early studies [16], there is a major difficulty in establishing the Q^n speciation in thiosilicates from NMR due to (i) the small number of reference crystalline phases (Li_2SiS_3 and Li_4SiS_4) in comparison with corresponding oxides, as such phases usually serve for the NMR chemical shift identification, and (ii) the small chemical shift anisotropies in thiosilicates, which do not permit to distinguish between various Q^n geometries. As a result and in contrast with lithium silicates [76], the addition of Li_2S into SiS_2 leads only to small variations in the ^{29}Si chemical shift [77] so that the Q^n distribution with composition or temperature is almost unknown. One should also note that the alkali type and thermal history both affect the Q^n distribution, at least from a simulation viewpoint [44]. However, an interpretation from the NMR results seem to indicate that thiosilicates [41] display a binary model predominantly made of Q^4 (the base short-range order of SiS_2) and Q^2 species [16].

The calculated Q^n distribution of the simulated $g\text{-Li}_2\text{SiS}_3$ is given in Table IV, and one detects that the distribution covers all accessible Q^n structures, ranging from Q^4 (5.8%, typical of the base network SiS_2) to Q^0 (an isolated $\text{Li}_4^{\oplus}\text{SiS}_4^{\ominus}$ molecule) that is typical of short-range order of the corresponding crystalline phase [37] Li_4SiS_4 . However, a variety of

other motifs are present, including Q^2 species (35.4%), which represent the unique geometry in $e\text{-Li}_2\text{SiS}_3$ and in an ideal chemical model (100%). The calculated statistics appears to be somewhat different from the proposed NMR statistics [16] but one has, once again, to remind that the distinction from NMR between the various Q^n species is difficult in $\text{Li}_2\text{S-SiS}_3$ glasses given the close chemical shifts between reference Q^2 and other crystalline reference compounds. We finally note that a broad distribution of Q^n species is usually found in modified oxides with cations of small sizes [45], and this situation seems to be met in the present thiosilicates as well, as also confirmed by a topological model [29].

An additional quantity permits to discuss the behavior of Li_2SiS_3 and compare with corresponding alkali oxides such as Li_2SiO_3 or Na_2SiO_3 . A concentration conservation law [29] permits to write that

$$R = \frac{2x}{1-x} = \sum_n (n-4)p_n \quad (14)$$

and $R = 1$ for $g\text{-Li}_2\text{SiS}_3$ if all Li atoms participate only to one Q^n with probability p_n . Using our calculated statistics (Table IV), we find that $R = 2.13$, and this value is somewhat larger than the one determined, e.g., for Li silicates ($R = 1.97$ [65]). The origin of the difference arises from a more important fraction of Q^1 and Q^0 units that are less present in lithium silicates [65], which furthermore exhibit a Li coordination number [78] of about $n_{\text{LiO}} = 2-3$. This defines a certain number of possible pairing arrangements [79], which also constrain the Q^n population.

5. BS and NBS distances

Silicates display a marked difference around the Si atom, depending whether the oxygen atom is bridging (BO, i.e., connecting two tetrahedra) or nonbridging (NBO, related to an alkali ion). These features have been observed in $\alpha\text{-Na}_2\text{Si}_2\text{O}_5$ and Na_2SiO_3 crystals [80,81], and have been also detected in simulated glasses [65,82] where the bond distance difference is of about 0.08–0.1 Å, i.e., the Si-BO is slightly longer than the Si-NBO bond length. For the specific case of lithium silicates [83] corresponding calculated distances are found to be of 1.64 Å and 1.57 Å, respectively, albeit not necessarily recovered from experiments [79,84,85]. It is therefore tempting to verify if such features are also present in corresponding sulfides.

Figure 9 represents the Si-BS and Si-NBS bond-distance distribution. Several comments can be made. First, as in lithium silicates [83] we do find a bond length difference since the average Si-BS and Si-NBS are found to be 2.12 Å and 2.09 Å in $g\text{-Li}_2\text{SiS}_3$, respectively, i.e., the difference is only of 0.03 Å which is substantially smaller than for corresponding silicates. The same analysis for the crystalline $e\text{-Li}_2\text{SiS}_3$ leads to an increased difference (0.09 Å) that mimics the one found in silicates [80,81] but we note that the overall Si-S bond distance also increases between the crystalline and the amorphous state (see Table II). The physical origin of Si-bridging atom (O,S) vs Si-nonbridging atom (O,S) bond distance difference is common to silicates and thiosilicates, and is linked with the influence of the lithium ions on the neighboring charges and the Si-NBS ionic-covalent character

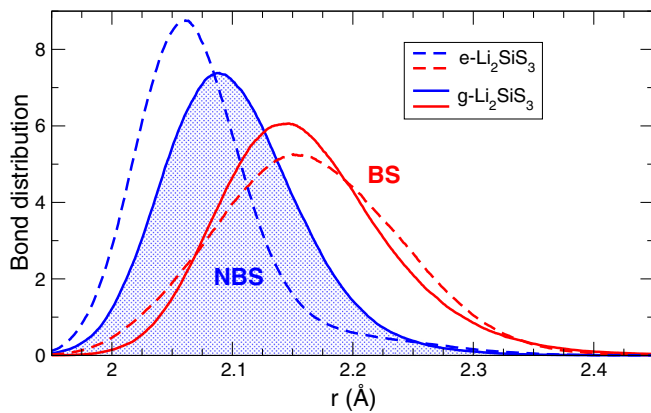


FIG. 9. Calculated distribution of Si-BS (red) and Si-NBS (blue) bond distances in $g\text{-Li}_2\text{SiS}_3$ (solid lines) and $e\text{-Li}_2\text{SiS}_3$ (broken lines) at 300 K.

of the bonding that modifies the electronic structure of next neighbor silicon atoms. For the present sulfides, since the electronegativity difference with Li is smaller [86] ($\Delta\chi_{\text{Li-S}} = 1.60$ and $\Delta\chi_{\text{Li-O}} = 2.46$), one expects to see charge separation (i.e., ionic character) reduced with a possible reduced alteration of the Si environment. This appears to be especially present once the disordered atomic structure permits various arrangements of short-range order elements.

IV. SUMMARY AND CONCLUSIONS

Here we have established the force-field parameters for crystalline and glassy Li_2SiS_3 , a material of current interest given its importance as attractive solid electrolyte for all solid-state batteries applications with conductivities of the order of $10^{-3} \Omega^{-1} \text{cm}^{-1}$. Alternatively, it is considered as a very interesting base material that can be used for further

alloying (e.g., $\text{P}_2\text{S}_5\text{-SiS}_2\text{-Li}_2\text{S}$) in the search for a continuous improvement of ion conduction. The force-field uses a Buckingham form, and is able to describe both reported crystalline phases $m\text{-Li}_2\text{SiS}_3$ and $e\text{-Li}_2\text{SiS}_3$ for which we have provided the elastic properties. After melting and quenching the liquid to a glass, we have investigated the structural properties. The obtained structure models are found to display a very satisfying agreement with reported structure functions [pair correlation $g(r)$ and structure factor $S(k)$] from neutron or x-ray scattering experiments. Our results clearly indicate a network that is predominantly tetrahedral in character with the salient phenomenology already encountered in the archetypal alkali silicate glasses, i.e., a base network disruption upon Li addition that leads to the growing presence of nonbridging sulfur having in its vicinity Li atoms, a Q^n population that is more complex than established from simple random or chemistry-based bond models, and a Li coordination number of 3 that is compatible with experimental findings [25] but smaller than the one found in corresponding silicates. Intermediate range order is rather limited as ring population for the (Si,S) network is only detected for sizes $n > 8$.

Taken together, these force-field parameters should now be used to elucidate the dynamics in order to relate structural features typical of thiosilicates to ion conduction. This work is in progress.

ACKNOWLEDGMENTS

M.M. acknowledges Chaire d'Excellence UNAM-Sorbonne Université for financial support, and repeated funding from CNRS and Sorbonne Université. Ongoing discussions with Andrea Piarristeguy, Annie Pradel, Gerardo Naumis, Hugo Flores-Ruiz, and Søren Sørensen are gratefully acknowledged. This work is dedicated to the memory of the late Pr. Michel Ribes from Université de Montpellier (France), in recognition of his valuable contribution on ion-conducting glasses, and, specifically on the present Li_2SiS_3 system [12].

- [1] M. Weiss, R. Ruess, J. Kasnatscheew, Y. Levartovsky, N. R. Levy, P. Minnmann, L. Stolz, T. Waldmann, M. Wohlfahrt-Mehrens, D. Aurbach *et al.*, *Adv. Energy Mater.* **11**, 2101126 (2021).
- [2] J.-M. Tarascon and M. Armand, *Nature (London)* **414**, 359 (2001).
- [3] C. Masquelier, *Nat. Mater.* **10**, 649 (2011).
- [4] Z. A. Grady, C. J. Wilkinson, C. A. Randall, and J. C. Mauro, *Front. Energy Res.* **8**, 218 (2020).
- [5] H. Eckert, Z. Zhang, and J. H. Kennedy, *Chem. Mater.* **2**, 273 (1990).
- [6] F. Mizuno, A. Hayashi, K. Tadanaga, and M. Tatsumisago, *Adv. Mater.* **17**, 918 (2005).
- [7] K. Mori, T. Ichida, K. Iwase, T. Otomo, S. Kohara, H. Arai, Y. Uchimoto, Z. Ogumi, Y. Onodera, and T. Fukunaga, *Chem. Phys. Lett.* **584**, 113 (2013).
- [8] K. Ohara, A. Mitsui, M. Mori, Y. Onodera, S. Shiotani, Y. Koyama, Y. Orikasa, M. Murakami, K. Shimoda, K. Mori *et al.*, *Sci. Rep.* **6**, 21302 (2016).
- [9] W. H. Smith, S. A. Vaselabadi, and C. A. Wolden, *Mater. Today Commun.* **35** 105574 (2023).
- [10] K. Mori, K. Iwase, Y. Oba, K. Ikeda, T. Otomo, and T. Fukunaga, *Solid State Ionics* **344**, 115141 (2020).
- [11] A. Pradel and A. Piarristeguy, *Comptes Rendus. Géoscience* **354**, 79 (2022).
- [12] A. Pradel and M. Ribes, *Solid State Ionics* **18-19**, 351 (1986).
- [13] J. Kennedy, *Mater. Chem. Phys.* **23**, 29 (1989).
- [14] D. Foix, D. Gonbeau, G. Taillades, A. Pradel, and M. Ribes, *Solid State Sci.* **3**, 235 (2001).
- [15] D. Foix, H. Martinez, A. Pradel, M. Ribes, and D. Gonbeau, *Chem. Phys.* **323**, 606 (2006).
- [16] H. Eckert, J. H. Kennedy, A. Pradel, and M. Ribes, *J. Non-Cryst. Solids* **113**, 287 (1989).
- [17] S. Kondo, K. Takada, and Y. Yamamura, *Solid State Ionics* **53-56**, 1183 (1992).
- [18] A. Hayashi, S. Hama, H. Morimoto, M. Tatsumisago, and T. Minami, *J. Am. Ceram. Soc.* **84**, 477 (2001).
- [19] H. Peng, X. Ma, Z. Fan, and Y. Liang, *J. Chin. Ceramic Soc.* **34**, 1270 (2006).
- [20] C. Angell, *Solid State Ionics* **9-10**, 3 (1983).
- [21] C. Angell, *Solid State Ionics* **18-19**, 72 (1986).

- [22] M. Seshasayee and K. Muruganandam, *Solid State Ionics* **91**, 285 (1996).
- [23] K. Muruganandam and M. Seshasayee, *Solid State Commun.* **95**, 499 (1995).
- [24] D. L. Price and A. J. Ellison, *J. Non-Cryst. Solids* **177**, 293 (1994).
- [25] J. H. Lee, A. Pradel, G. Taillades, M. Ribes, and S. R. Elliott, *Phys. Rev. B* **56**, 10934 (1997).
- [26] S. Elliott, *Solid State Ionics* **105**, 39 (1998).
- [27] A. Dive, C. Benmore, M. Wilding, S. Martin, S. Beckman, and S. Banerjee, *J. Phys. Chem. B* **122**, 7597 (2018).
- [28] M. Micoulaut, *Comptes Rendus de l'Académie des Sciences Série II* **316**, 1679 (1993).
- [29] M. Micoulaut and R. Kerner, *J. Phys.: Condens. Matter* **9**, 2551 (1997).
- [30] A. Pedone, G. Malavasi, M. C. Menziani, A. N. Cormack, and U. Segre, *J. Phys. Chem. B* **110**, 11780 (2006).
- [31] R. D. Oeffner and S. R. Elliott, *Phys. Rev. B* **58**, 14791 (1998).
- [32] S. Tsuneyuki, H. Aoki, M. Tsukada, and Y. Matsui, *Phys. Rev. Lett.* **64**, 776 (1990).
- [33] J. D. Gale, *Philos. Mag. B* **73**, 3 (1996).
- [34] J. D. Gale, *J. Chem. Soc., Faraday Trans.* **93**, 629 (1997).
- [35] J. D. Gale and A. L. Rohl, *Mol. Simul.* **29**, 291 (2003).
- [36] A. Weiss and G. Rocktäschel, *Z. Anorg. Allg. Chem.* **307**, 1 (1960).
- [37] B. T. Ahn and R. A. Huggins, *Mater. Res. Bull.* **24**, 889 (1989).
- [38] B. T. Ahn and R. A. Huggins, *Solid State Ionics* **46**, 237 (1991).
- [39] B. T. Ahn and R. A. Huggins, *Mater. Res. Bull.* **25**, 381 (1990).
- [40] W. Huang, N. Matsui, S. Hori, K. Suzuki, M. Hirayama, M. Yonemura, T. Saito, T. Kamiyama, Y. Sasaki, Y. Yoon *et al.*, *J. Am. Chem. Soc.* **144**, 4989 (2022).
- [41] A. Pradel, G. Taillades, M. Ribes, and H. Eckert, *J. Non-Cryst. Solids* **188**, 75 (1995).
- [42] L. T. Kong, *Comput. Phys. Commun.* **182**, 2201 (2011).
- [43] J. Peters and B. Krebs, *Acta Crystallogr. Sec. B* **38**, 1270 (1982).
- [44] L. Deng and J. Du, *J. Chem. Phys.* **148**, 024504 (2018).
- [45] B. Mysen and P. Richet, *Silicate Glasses and Melts* (Elsevier, Amsterdam, 2018).
- [46] M. Micoulaut, *J. Phys.: Condens. Matter* **16**, L131 (2004).
- [47] J. F. Nye, *Physical Properties of Crystals: Their Representation by Tensors and Matrices* (Oxford University Press, Oxford, 1985).
- [48] T. Rouxel, *Comptes Rendus Mécanique* **334**, 743 (2006).
- [49] S. Hasan, K. Baral, N. Li, and W.-Y. Ching, *Sci. Rep.* **11**, 9921 (2021).
- [50] F. P. McGrogan, T. Swamy, S. R. Bishop, E. Eggleton, L. Porz, X. Chen, Y.-M. Chiang, and K. J. Van Vliet, *Adv. Energy Mater.* **7**, 1602011 (2017).
- [51] Z. Deng, Z. Wang, I.-H. Chu, J. Luo, and S. P. Ong, *J. Electrochem. Soc.* **163**, A67 (2016).
- [52] H. Jabraoui, Y. Vaills, A. Hasnaoui, M. Badawi, and S. Ouaskit, *J. Phys. Chem. B* **120**, 13193 (2016).
- [53] A. Pedone, G. Malavasi, A. N. Cormack, U. Segre, and M. C. Menziani, *Chem. Mater.* **19**, 3144 (2007).
- [54] A. Sakuda, A. Hayashi, Y. Takigawa, K. Higashi, and M. Tatsumisago, *J. Ceram. Soc. Jpn.* **121**, 946 (2013).
- [55] B. Mantsi and M. Micoulaut, *J. Non-Cryst. Solids* **440**, 1 (2016).
- [56] B. Mantsi, M. Bauchy, and M. Micoulaut, *Phys. Rev. B* **92**, 134201 (2015).
- [57] Z. Liu, Y. Hu, X. Li, W. Song, S. Goyal, M. Micoulaut, and M. Bauchy, *Phys. Rev. B* **98**, 104205 (2018).
- [58] J. A. Zasadzinski, *J. Microsc.* **150**, 137 (1988).
- [59] B. Guillot and Y. Guissani, *J. Chem. Phys.* **119**, 11740 (2003).
- [60] K.-F. Hesse, *Acta Crystallogr., Sect. B: Struct. Crystallogr. Cryst. Chem.* **33**, 901 (1977).
- [61] E. Zintl, A. Harder, and B. Dauth, *Z. Elektrochem. Angew. Phys. Chem.* **40**, 588 (1934).
- [62] M. Bauchy and M. Micoulaut, *Phys. Rev. B* **83**, 184118 (2011).
- [63] O. Laurent, B. Mantsi, and M. Micoulaut, *J. Phys. Chem. B* **118**, 12750 (2014).
- [64] S. Chakraborty, P. Boolchand, and M. Micoulaut, *Phys. Rev. B* **96**, 094205 (2017).
- [65] J. Du and A. Cormack, *J. Non-Cryst. Solids* **349**, 66 (2004).
- [66] M. Bauchy and M. Micoulaut, *J. Non-Cryst. Solids* **357**, 2530 (2011).
- [67] M. Micoulaut, A. Piarristeguy, H. Flores-Ruiz, and A. Pradel, *Phys. Rev. B* **96**, 184204 (2017).
- [68] M. Tenhover, M. A. Hazle, and R. K. Grasselli, *Phys. Rev. Lett.* **51**, 404 (1983).
- [69] M. Tenhover, M. A. Hazle, and R. K. Grasselli, *Phys. Rev. B* **29**, 6732 (1984).
- [70] H. Eckert, Z. Zhang, and J. H. Kennedy, *J. Non-Cryst. Solids* **107**, 271 (1989).
- [71] S. Le Roux and P. Jund, *Comput. Mater. Sci.* **49**, 70 (2010).
- [72] S. V. King, *Nature (London)* **213**, 1112 (1967).
- [73] D. S. Franzblau, *Phys. Rev. B* **44**, 4925 (1991).
- [74] H. Flores-Ruiz and M. Micoulaut, *J. Chem. Phys.* **157**, 054507 (2022).
- [75] O. L. Alderman, G. Ferlat, A. Baroni, M. Salanne, M. Micoulaut, C. Benmore, A. Lin, A. Tamalonis, and J. Weber, *J. Phys.: Condens. Matter* **27**, 455104 (2015).
- [76] H. Maekawa, T. Maekawa, K. Kawamura, and T. Yokokawa, *J. Non-Cryst. Solids* **127**, 53 (1991).
- [77] Y. Tokuda, T. Uchino, and T. Yoko, *J. Non-Cryst. Solids* **282**, 256 (2001).
- [78] N. Umesaki, M. Takahashi, M. Tatsumisago, and T. Minami, *J. Mater. Sci.* **28**, 3473 (1993).
- [79] G. S. Henderson, *Can. Mineral.* **43**, 1921 (2005).
- [80] A. Pant, *Acta Crystallogr., Sect. B: Struct. Crystallogr. Cryst. Chem.* **24**, 1077 (1968).
- [81] W. T. McDonald and D. Cruickshank, *Acta Crystallogr.* **22**, 37 (1967).
- [82] X. Yuan and A. N. Cormack, *J. Non-Cryst. Solids* **283**, 69 (2001).
- [83] J. Du and L. R. Corrales, *J. Chem. Phys.* **125**, 114702 (2006).
- [84] H. Uhlig, M. J. Hoffmann, H.-P. Lamparter, F. Aldinger, R. Bellissent, and S. Steeb, *J. Am. Ceram. Soc.* **79**, 2833 (1996).
- [85] A. C. Hannon, B. Vessal, and J. M. Parker, *J. Non-Cryst. Solids* **150**, 97 (1992).
- [86] L. Pauling, *J. Chem. Education* **69**, 519 (1992).